Influence of Morphological Factors on Tensile Properties in the Pre-yield Region of Isotactic Polypropylenes

Koh-hei NITTA[1,†] and Naoto YAMAGUCHI[2]

[1]*Department of Chemical Engineering, Graduate School of Natural Science and Technology, Kanazawa University, Kakuma-machi, Kanazawa 920-1192, Japan*
[2]*School of Materials Science, Japan Advanced Institute of Science and Technology, Asahidai, Tatsunokuchi, Ishikawa 923-1292, Japan*

ABSTRACT: We examined the molecular and structural variables that govern tensile properties of isotactic polypropylene forming spherulitic morphology. The polypropylenes were crystallized in such a manner as to develop as a wide range as possible in the values of the independent structural variables that describe the solid state. The initial deformations depend strongly on the amorphous regions but are independent of the spherulite size and lamellar thickness. At yield point the lamellae within spherulites were found to be fragmented and replaced by a highly oriented fibrous structure in the post-yield region. [DOI 10.1295/polymj.38.122]
KEY WORDS Isotactic Polypropylene / Tensile Properties / Morphology / Spherulite /

Semicrystalline polymers such as polyethylene and polypropylene contain both a liquid-like amorphous phase and an ordered crystalline phase. When solidified from the melt, these polymers show spherulitic structure, in which the crystalline lamellae composed of folded chains radiate from its center and the amorphous phases reside in the interlamellar regions in the form of tie chains, loop chains, cilia chains, and floating chains. In addition, the spherulite is filled with the lamellae in such a way that a constant long period is approximately maintained.

The tensile properties of semicrystalline polymers showing spherulitic structure have been received a great deal of attention because of their scientific interest as well as practical importance. However, the molecular and structural mechanism underlying the deformation process is not well clarified yet. Essentially mechanical properties of these spherulitic materials are controlled by molecular morphology which depends largely on molecular constitution such as molecular weight and the structural regularity of the chain as well as crystallization conditions.[1] The morphology of semicrystalline polymers can be simplified by various levels of hierarchy in structure such as crystalline thickness, amorphous layer thickness, the size of spherulite and the structural organization in the residual amorphous region.[2] These diversity and independencies of these structural variables make it difficult to provide a molecular or structural interpretation for tensile behavior as suggested by Mandelkern *et al.*[2–5] In order to obtain a better understanding to the tensile behavior of semicrystalline polymers, these variables should be isolated and their individual roles assessed. Recently, this strategy has also been used in studies of tensile deformation of several polyethylenes.[3,4] The present work is restricted to isotactic polypropylenes which are one of the most widely used polymers and expected to be further enhanced performance in the future.[5] The objective is to explore the structural variables that govern tensile behavior for isotactic polypropylenes with a high isotacticity. The independent structural variables are widely varied by controlling the molecular constitution and the crystallization conditions. For the purpose, the polymers studied include homopolymers having a wide range of molecular mass and the binary blends with an ethylene-1-hexene copolymer which is miscible with polypropylene chains in the amorphous state.[6–8] These samples were crystallized in such a manner so as to develop as wide range as possible in structural parameters such as crystalline thickness, amorphous layer thickness, and the size of spherulites which are considered to be core elements of the structural morphology of bulk-crystallized polymers.

EXPERIMENTAL

Materials

The starting materials used in this work were isotactic polypropylenes with a high isotacticity (99–98%) and different molecular weights. The molecular characteristics are summarized in Table I. The end-numeral of the PP in Table I denotes the molecular weight M_w in 10^4.

[†]To whom correspondence should be addressed (Tel: +81-76-234-4818, Fax: +81-76-264-6220, E-mail: nitta@t.kanazawa-u.ac.jp).

Table I. Molecular characteristics of samples

| Sample | Composition (mol %) | | $M_w \times 10^{-4}$ | M_w/M_n |
	Ethylene	1-Hexene		
PP20	—	—	20.3	6.22
PP26	—	—	26.0	5.65
PP38	—	—	37.7	8.14
PP49	—	—	49.0	4.38
EHR	40.8	59.2	82.6	1.79

The endnumeral of the PP denotes the molecular weight M_w, in 10^4.

Sample Preparation

The samples were compression molded in a laboratory hot press at $210\,°C$. The samples were completely melted for 5 min between two aluminum plates prior to the application of a pressure of 10 MPa to produce films of approximately 0.2 to 0.5 mm thick. The molten films were allowed to equilibrate under pressure for 5 min prior to cooling. On removal from the press, the samples were plunged directly into a water bath maintained at the appropriate temperature of 0, 30,

60, and $100\,°C$.

The amorphous layer thickness was controlled by the addition of a rubbery ethylene-1-hexene copolymer (EHR) into PP26 sample on the basis of the experimental fact that EHR molecules are dissolved in the amorphous region of PP.[6–8] The molecular characteristics of the EHR sample are also presented in Table I. The blends of PP26 and EHR were mixed in a solution of xylene at $110\,°C$. The blend compositions of PP/EHR were 97/3, 95/5, 90/10, 80/20, and 70/30 (w/w). The samples were pressed in the hot press to be used for measurements. The film specimens of the PP/EHR system were prepared by quenching the pressed film into an ice water bath ($0\,°C$) after being melted in the hot press.

The structural characteristics of the samples that were studied are summarized in Table II. The nomenclature used in this work is as follows: Q denotes the quenched film and its numeral the quenching temperature in $°C$, and A denotes the annealed film in which the corresponding quenched film is annealed at $100\,°C$

Table II. Structural characteristics of samples

Sample	T_m [a] /K	ρ [b] /kg m^{-3}	χ_v [c] /%	L_p [d] /nm	L_c [e] /nm	L_a [f] /nm	R [g] /μm
Q0-PP20	438	903.1	59.9	11.3	6.77	4.54	3.81
Q100-PP20	440	907.8	63.7	13.8	8.78	4.65	7.62
A0-PP20	440	906.2	65.6	13.7	8.99	4.71	5.36
A100-PP20	440	909.3	67.4	13.9	9.37	4.53	13.9
Q0-PP26	443	900.4	56.6	11.1	6.29	4.81	4.42
Q30-PP26	443	905.6	62.2	11.9	7.40	4.50	4.76
Q60-PP26	444	907.1	64.6	12.1	7.82	4.28	7.17
Q100-PP26	444	910.4	68.3	13.9	9.49	4.41	10.4
A0-PP26	444	909.3	67.4	13.5	9.10	4.40	6.77
A30-PP26	444	910.3	68.3	15.6	10.7	4.95	8.15
A60-PP26	444	910.3	68.3	15.6	10.7	4.95	11.6
A100-PP26	443	912.0	70.7	15.5	11.0	4.54	15.6
Q0-PP38	438	898.0	53.7	10.6	5.69	4.91	3.11
Q100-PP38	441	906.0	63.4	13.5	8.60	4.91	6.75
A0-PP38	439	904.5	61.6	14.1	8.31	5.19	5.13
A100-PP38	440	909.8	68.0	15.0	10.2	4.80	14.7
Q0-PP49	438	897.7	53.3	10.6	5.65	4.95	3.28
Q100-PP49	440	905.7	63.0	13.6	9.37	5.46	7.15
A0-PP49	439	903.1	59.8	14.6	8.14	4.39	3.58
A100-PP49	440	907.6	65.4	14.3	9.35	4.95	13.9
A0-PP/EHR(97/3)	442	910.5	68.9	14.2	9.79	4.42	4.63
A0-PP/EHR(95/5)	442	908.7	66.7	14.7	9.79	4.48	6.75
A0-PP/EHR(90/10)	443	905.1	62.3	15.2	9.44	5.71	5.25
A0-PP/EHR(80/20)	443	900.1	56.2	15.8	8.91	6.94	7.62
A0-PP/EHR(70/30)	442	894.9	49.6	17.1	8.51	8.63	7.15

[a]Melting temperature; [b]Density; [c]Crystallinity in volume fraction; [d]Long period; [e]Lamellar thickness; [f]Amorphous layer thickness; [g]Spherulite radius.

for 24 h. The melting temperature in Table II is the peak melting temperature on DSC curves at a scanning rate of 10 °C/min.

Structural Characterization

The densities were measured using a floating method at 30 °C. The binary medium prepared from various ratios of distilled water and ethylalchohol was used for the measurements. The degree of crystallinity in volume fraction χ_v was calculated using 936 and 854 kg/m^3 for the densities of the crystalline and amorphous regions:[9,10]

$$\chi_v = \frac{\rho - \rho_a}{\rho_c - \rho_a} \qquad (1)$$

where ρ is the density of the sample, ρ_a is the density of amorphous component, and ρ_c is the density of crystal component.

The size of spherulite was determined from small angle light scattering measurements in which a 2 mW He–Ne laser was used as a light source (the wavelength of light $\lambda = 632.8$ nm). The detector used was a photomultiplier that can rotate horizontally around a film specimen of 100 μm thick to scan polar scattering angles θ. The scattered light intensity under the cross-polarization condition was measured at the azimuthal angle $\mu = 45°$ at a fixed step of 0.1°. The spherulite radius R was evaluated using the following equation:

$$R = \frac{U_m \lambda}{4\pi n \sin(\theta_m/2)} \qquad (2)$$

where θ_m is the scattering angle at which the intensity is a maximum, $n\ (= 1.49)$ is the refractive index of PP and $U_m = 4.1$.[11]

The small angle X-ray scattering (SAXS) measurement was performed with a point focusing optics and an one-dimensional position sensitive proportional counter (PSPC) with an effective length of 10 cm. The CuKα radiation supplied by a MAC Science M18X generator operating at 40 kV and 30 mA was used throughout. The SAXS profiles for all samples after an appropriate correction (*e.g.* Lorentz correction) were characterized by one or more diffuse peak, and the maximum peak was converted into the long period L_p according to Bragg's law. Assuming that the crystalline lamellae are spaced filling with a single population of thickness, the lamellar thickness L_c can be calculated by using the following relation:

$$L_c = \chi_v L_p \qquad (3)$$

Tensile Measurements

Dumbbell-shaped specimens were used for the tensile tests. They were cut from the compression molded films of 500 μm thickness with a cutter and have a

gauge length of 10 mm and a width of 4 mm. The samples were elongated at room temperature (24 °C) and at a constant elongation rate of 1, 20, 50, and 100 mm/min using a Shimadzu AGS-5kN. The tensile stress was determined from dividing the tensile load by the initial cross section and the tensile strain was calculated from the ratio of the increment of the length between clamps to the initial gauge length. In this work, the yield stress σ_y was defined as a maximum stress in the stress-strain curve and the Young's modulus E_Y was evaluated from the initial slope. The yield energy U_y, which is defined as the mechanical energy dissipated for yielding to take place,[12] was here defined as the area under the stress–strain plot from the origin to the stress drop. It is likely that U_y corresponds to the elastic-strain energy required for the crystalline lamellae constructing spherulites to be fragmented. The actual values of these mechanical parameters reported here are mean averages of the parameters obtained for the 5 to 10 samples of each film.

Rheo-optical Measurements

Rheo-optical techniques[13–15] afford information on the strain dependence not only of stress but also of optical quantities associated directly with the structure or molecular morphology. The techniques were developed extensively for crystalline polymers to investigate the molecular deformation mechanism underlying the tensile elongation. In this work, infrared dichroism was measured simultaneously with tensile deformation at a constant rate of elongation to investigate the chain orientation behavior.

A tensile tester was set in Fourier-transform infrared spectrometer (JASCO FT-IR500) in such a way to allow infrared beam through a film specimen mounted on the tensile tester. The tensile tester was specially designed for upper and lower clamps to symmetrically move from the central point of the film so that the beam spot remains at the initial position during a whole stretching. The elongation speed was 1 mm/min in all cases. The dumbbell-shaped specimens of 100 μm thickness were used. In this work, the intensities of 998 cm^{-1} band, which is associated with CH$_3$ rocking mode as coupled with C–CH$_3$ stretching mode, was measured as a function of time or strain every 10 s. Using the dichroic ratio of the band, we estimated the orientation function of crystal c-axis as described previously.[8]

Differential Scanning Calorimetry Measurements

In order to examine the lamellar fragmentation process during elongation, we performed the differential scanning calorimetry (DSC) measurements of a deformed specimen. DSC was carried out using a Mettler DSC820 that was calibrated for temperature
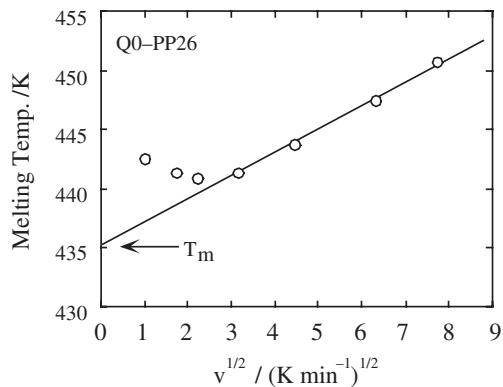
Figure 1. Melting points of a quenched PP film (Q0-PP26) as a function of square root of heating rate.

Figure 2. Stress–strain curves for A30-PP26, A60-PP26, and A100-PP26. These PP samples have similar lamellar and interlamellar thickness but different spherulite radius from 8 to 16 μm.

and melting enthalpy using indium as a standard. The melting temperature obtained from DSC measurements depends on the heating rate because the changes in the crystalline morphology occurs during heating. Thus, the melting temperature extrapolated to the zero heating rate is related with the crystalline state or crystallite size of the samples. According to Rodriguez-Cabello *et al.*[16] the true melting temperature T_m for a given crystalline structure of a polypropylene film can be obtained by extrapolation of the linear sections of the resulting plot of the apparent melting temperature against the square root of the heating rate $V^{1/2}$ to $V = 0$. Figure 1 exemplifies melting points of a quenched PP film plotted against $V^{1/2}$. This study was made for the samples quickly cut from the deformed specimen just after a constant rate of elongation (1 mm/min). The samples sealed in aluminum pans were heated from 100 to 200 °C at a scanning rate of 1 to 100 °C/min under the nitrogen atmosphere.

The deviation between the true melting temperature T_m and the equilibrium melting temperature T_m^0 can be given by the Thompson–Gibbs equation of the form:

$$T_m = T_m^0\left(1 - \frac{2\sigma_e}{\Delta H_f L_c} - \frac{4\sigma_l}{\Delta H_f \lambda_c}\right) \quad (4)$$

where σ_e is the free surface energy of folding plane, σ_l is the free surface energy of the crystal side surface, L_c is the longitudinal dimension of crystal (lamellar thickness), λ_c is the lateral dimension of the lamella, ΔH_f is the heat of fusion per volume. Since the stretching process at room temperature in the pre-yield region has no ability to drastically change the lamellar thickness L_c, the changes in true melting temperature can be converted into the changes in lateral lamellar size by using the following equation derived from eq 4:

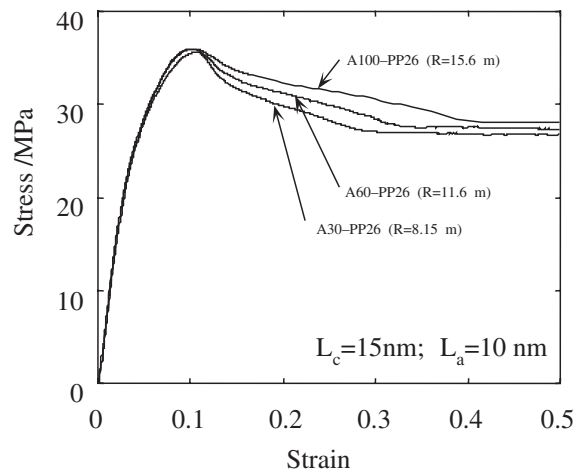$$\frac{1}{\lambda_c^0} - \frac{1}{\lambda_c} = \frac{\Delta H_f}{4\sigma_l T_m^0}[T_m - T_{m0}] \quad (5)$$

where λ_c^0 and T_{m0} are the lateral lamellar width and melting temperature of an undeformed PP sample, and λ_c and T_m are those of the deformed one. According to published data,[17–19] the values of $\Delta H_f = 1.96 \times 10^8$ J/m^3, $\sigma_l = 11.5 \times 10^{-3}$ J/m^2, and $T_m^0 = 481$ K were used in this work.

RESULTS AND DISCUSSION

Tensile Properties

Three samples such as A30-PP26, A60-PP26, and A100-PP26 were chosen for the investigation on the effects of spherulite radius on stress–strain behavior. As shown in Table II, these samples have the similar lamellar thickness (*ca.* 11 nm) and the similar amorphous layer thickness (4.5–5.0 nm), leading to the crystallinity of 68%, but the different spherulite radius from 8 to 16 μm. The examination of stress–strain curves of these PP samples as shown in Figure 2 clarifies that there is no influence of the spherulite size on the tensile behavior prior to yield. Thus, these samples delineate the same stress–strain curves up to the yield point. The insensitivity to the size of spherulite is theoretically confirmed. Previously, Nitta[20] investigated an affine deformation of an ideal spherulite model in which the crystalline lamellae are assumed to be rigid plates and the amorphous regions resides in the interlamellar regions in the forms of floating chains and tie chains according to the morphological feature of spherulitic polymers. The theoretical stress–strain curve of a spherulite can qualitatively calculated based on a consideration of changes in conformational free energy in the tie chains and floating chains located between the rigid plates. According to the previous theoretical treatment, the stress–strain curve of a spherulite was found to be independent of the radius
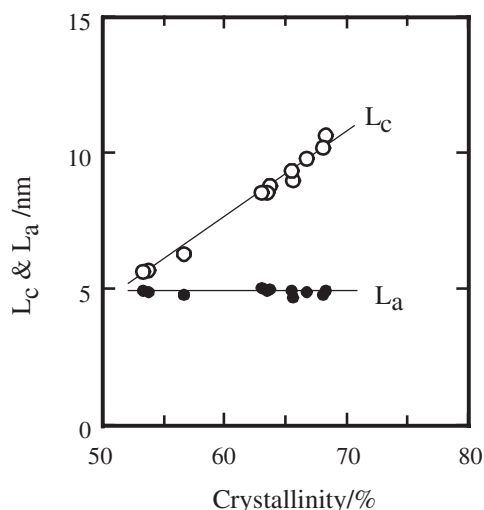
Figure 3. Crystallinity dependence of lamellar thickness L_c and amorphous layer thickness L_a for PP samples.

Figure 4. Lorentz-corrected X-ray intensities of A0-PP26 and A0-PP/EHR blends plotted against the wave number.

Figure 5. Lamellar thickness L_c and amorphous layer thickness L_a A0-PP26 and A0-PP/EHR blend plotted against the EHR content.

of the spherulite when the crystalline thickness and the interlamellar thickness within the spherulite are fixed.

Some PP samples having the amorphous layer thickness of 4.7–5.1 nm were chosen for the study on the effect of lamellar thickness on tensile behavior. As is confirmed from Figure 3, in the set of PP samples the amorphous layer thickness L_a remains constant (*ca.* 5 nm) but their lamellar thicknesses are in the range from 5 to 13 nm. In order to investigate the effects of amorphous layer thickness on tensile properties, we chosen a series of PP/EHR blends and pure A0-PP26. Figure 4 shows the Lorentz-corrected SAXS intensities of A0-PP26 and A0-PP/EHR blends plotted against the wave number s ($= 2/\lambda \sin \theta$)) in which 2θ is the scattering angle and λ is the X-ray wavelength ($= 0.1542$ nm). The angular position of the intensity peak shifts toward larger s as the EHR content increases in the PP/EHR blends, suggesting the incorporation of EHR molecules into amorphous regions of the iPP. The maximum point in the SAXS curves yields the average long period. The lamellar thickness and the amorphous layer thickness were determined from the data of volume fraction of crystallinity and the SAXS long periods (see Table II).

As shown in Figure 5, in the set of PP/EHR samples the crystalline lamellar thickness remains constant (*ca.* 9–10 nm) but their amorphous layer thickness linearly increases from 5 to 10 nm with increasing the EHR content, demonstrating that EHR molecules are completely incorporated into the amorphous regions of PP as already demonstrated by Yamaguchi and Nitta *et al.*[6–8,21] In addition, considering that the density of pure EHR samples is almost the same with that of amorphous PP phase, the PP/EHR blends can
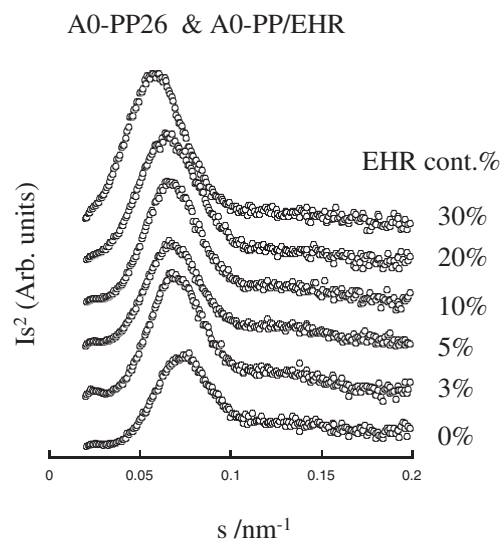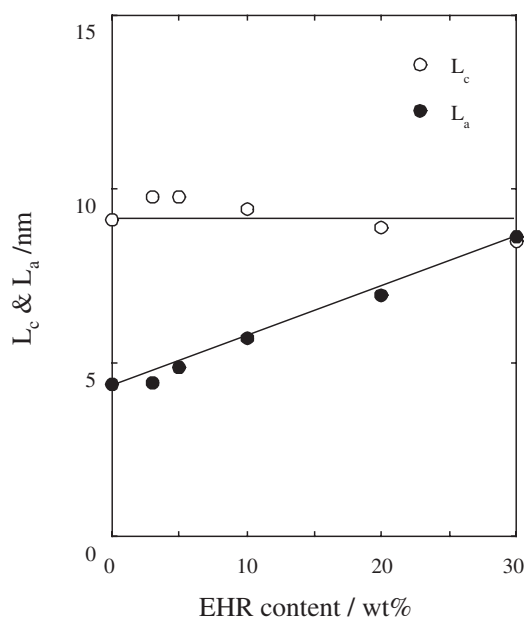
be regarded to be PP samples having different amorphous layer thicknesses. This means that EHR molecules act as floating chains in the interlamellar regions, leading to the increase of the interlamellar distance as well as to the reduction of the probability for forming tie molecules.

The yield stress σ_y and the Young's modulus E_Y of these PP films are plotted against the lamellar thickness in Figures 6a and 7a. These films have a constant lamellar thickness of about 10 nm but their amorphous layer thicknesses are range from 5 to 9 nm. The yield stress σ_y and the Young's modulus E_Y of these films are plotted against the amorphous layer thickness L_a
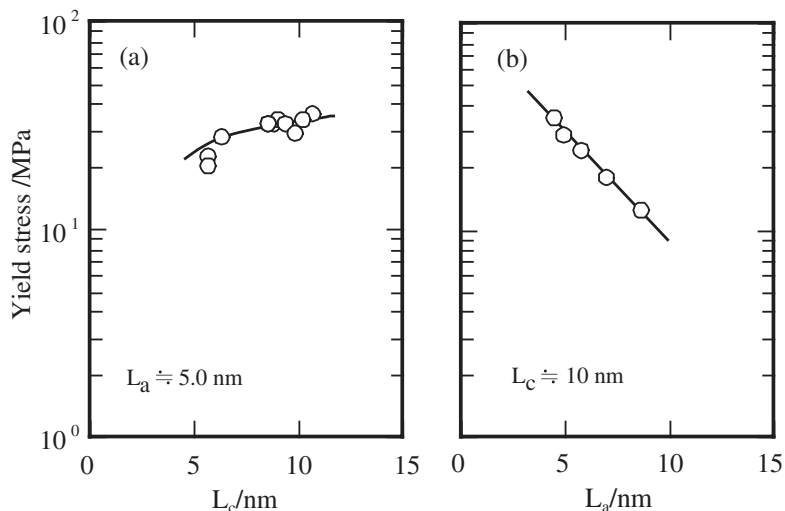
Figure 6. Influence of (a) lamellar thickness and (b) amorphous layer thickness on yield stress.
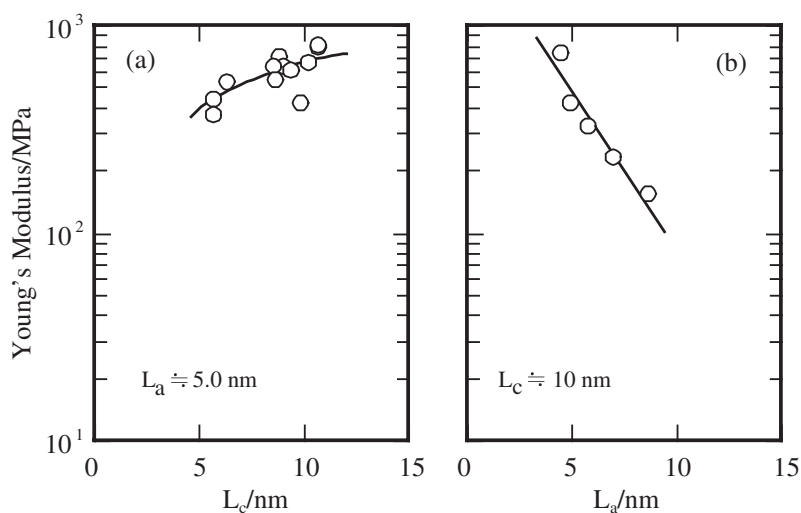

Figure 7. Influence of (a) lamellar thickness and (b) amorphous layer thickness on Young's modulus.

in Figures 6b and 7b.

As seen in Figures 6 and 7, the higher crystallinity (fraction of crystal component) samples show a higher modulus and yield stress. However, the effect of amorphous layer thickness was found to be much greater than the effect of the lamellar thickness. It seems that PP samples showing a constant amorphous layer thickness exhibited a similar stress–strain behavior in the pre-yield region. The strong dependence of amorphous layer thickness on modulus and stress level in the pre-yield region can be explained by considering that the external stress is concentrated to the amorphous region. This is because the rigidity of crystalline lamellae is much greater than that of amorphous region, the deformation of the amorphous phases dominantly affects on the modulus and stress level in the pre-yield region. Thus, the decrease in amorphous layer causes a greater strain to impose on the amorphous parts within the deformed spherulites because of the decrease in the

initial interlamellar spacing. In addition, the addition of EHR chains or the increase in the amorphous thickness directly reduces the amount of tie molecules playing a role in stress-transmitter and lower the overall stress level in the pre-yield region. Otherwise, the reduction in molecular mobility of PP in PP/EHR blends could influence the modulus and the stress levels of the blends.

The total yield energy U_y, which here was determined from the area under the stress–strain plot from the origin to the stress drop, tends to increase with increasing L_c but is independent of the amorphous layer thickness L_a or the addition of EHR (see Figure 8). This implies that the yield process is associated with the disintegration of lamellar crystals.

In Figure 9, the yield energies of the PP samples (A100-PP26, A60-PP26, and A30-PP26) with $L_c \cong$ 15 nm and $L_a \cong 10$ nm are plotted against the spherulite radius. It is likely that the spherulite radius is pro-
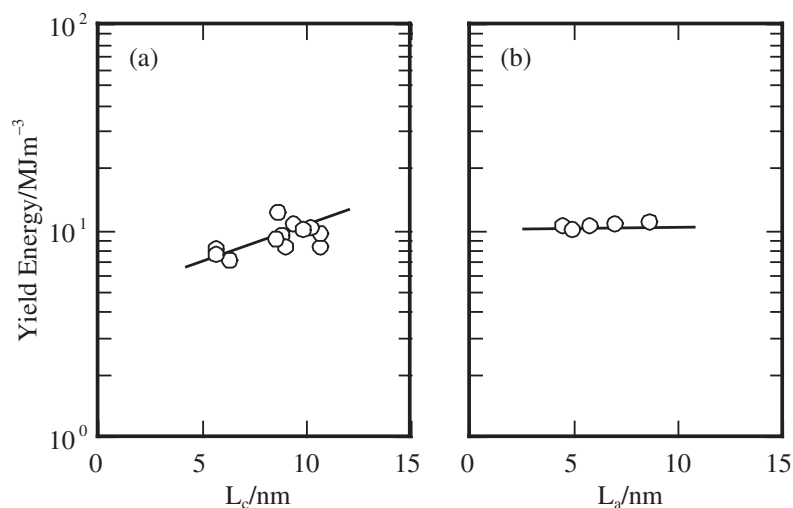
Figure 8. Influence of (a) lamellar thickness and (b) amorphous layer thickness on yield energy.
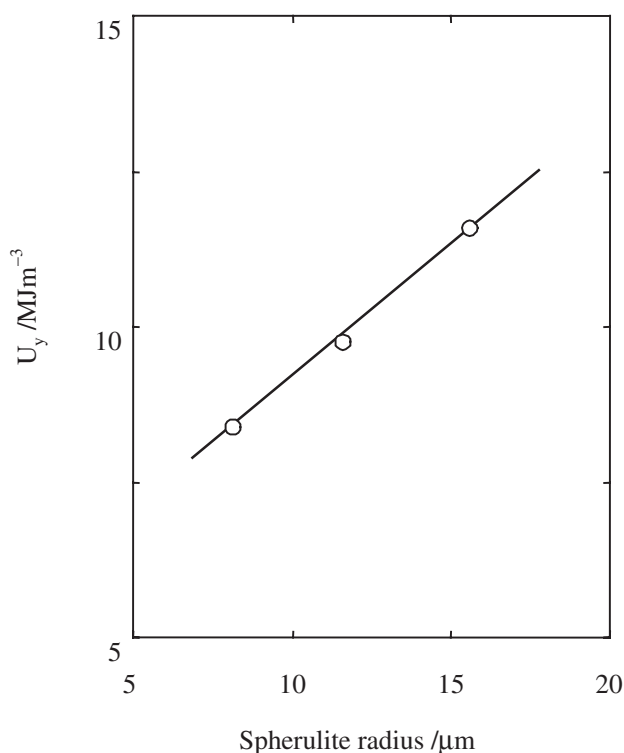

Figure 9. Dependence of the yield energy on the spherulite radius for A30-PP26, A60-PP26, and A100-PP26 having similar lamellar and interlamellar thicknesses.

portional to the lateral dimension λ_c of lamellae. Comparison with Figure 8 shows the relatively strong dependence of the radius of spherulite on U_y, suggesting that the total mechanical energy required for fragmentation of crystalline lamellae is closely related to their lateral dimension.

The important results that the relatively weak influence of crystallite thickness on the initial modulus and stress, and the strong influence on interlamellar spacing can be expressed by considering that the stress or strain concentrates on the amorphous regions because the modulus of amorphous phase is much lower than that of crystalline phase. The well-known results that Young's modulus and the stress level increase with increasing the degree of crystallinity can be attributed to the deformation imposed on the thinner interlamellar region.

Deformation Mechanism

In Figure 10, the orientation function of crystal *c*-axis and the changes in the lateral lamellar size are plotted against the tensile strain for Q0-PP26 film, including the stress–strain curve. In these figures, the dotted line at around 0.15 of the strain denotes the yield point and the dotted line at around 0.3 denotes the onset of necking process. In the first pre-yield region, the orientation function of *c*-axis decreases with increasing strain. Considering that in this region the spherulite was confirmed to be almost affinely deformed, the negative orientation can be explained by the following mechanism:[22] the lamellar orientation or the *a** or *b*-axis orientation forced by the deformation of spherulite caused the *c*-axis to orient perpendicular to the stretching direction. Moreover, as seen in Figure 10b, the lateral lamellar size is clearly unchanged until the yield point. This suggests that the spherulites are deformed accompanying no fragmentation of lamellae. Just after yield point, the lateral lamellar size drastically drops and the orientation function remains approximately constant until the onset of necking, indicating that the lamellar fragmentation process takes place at yield point. In the post-yield region in which the neck travels along the film specimen, the recovery of lateral lamellar size as well as the increase in the orientation of *c*-axis can be explained by the recrystallization process accompanied with the necking progression.
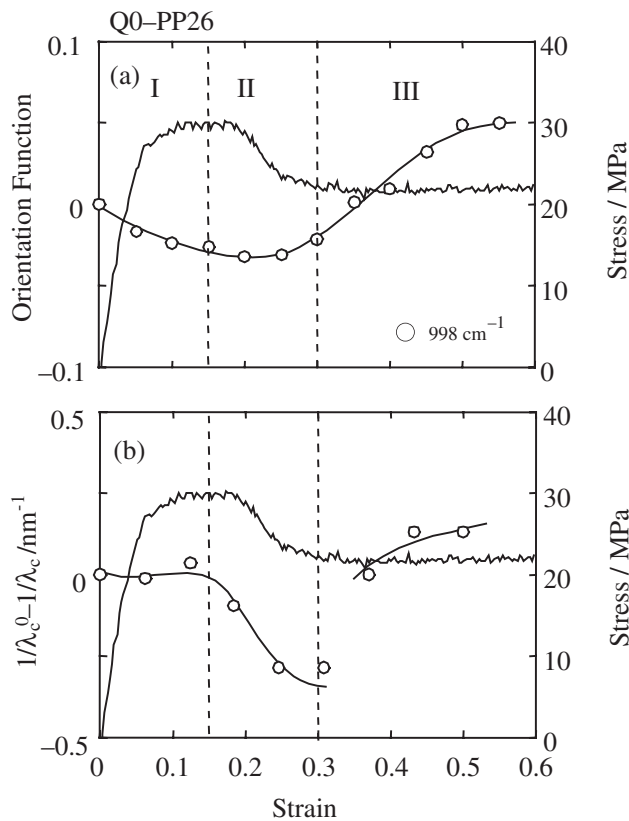
Figure 10. (a) Orientation function of *c*-axis and (b) changes in lateral lamellar size plotted against strain for Q0-PP26. The solid curves denote the stress–strain curves.

Figure 11. (a) Orientation function of *c*-axis and (b) changes in lateral lamellar size plotted against strain for A30-PP26. The solid curves denote the stress–strain curves.

Figures 11 and 12 compare the deformation processes for the PP samples having similar lamellar and interlamellar thicknesses but different spherulite sizes. In the initial strain region, the deformation mechanism is found to be independent of the radius of spherulite. For the sample having lager spherulite radius, the yielding region beyond the yield point becomes broader and the drop in the lateral lamellar size in the yielding region is enhanced. This is much likely because changes in the lateral lamellar size resulting from lamellar fragmentation can be considered to be proportional to their length.

The effects of interlamellar spacing on the orientation behavior were examined using the set of PP/EHR samples having different amorphous layer thicknesses but a constant lamellar thickness. The yield peak is more diffuse and poorly defined as the amorphous layer thickness increases as shown in Figure 13. Following the yield, an upswing in the orientation function is observed. Increase in the amorphous layer thickness lowers the slope of the orientation-strain relation. At the high amorphous layer thicknesses such as PP/EHR (70/30), no clear yield peak is observed and no lamellar fragmentation takes place as seen in Figure 14. In addition, the slight increase in the lateral lamellar size is observed at which a slight neck is ini-
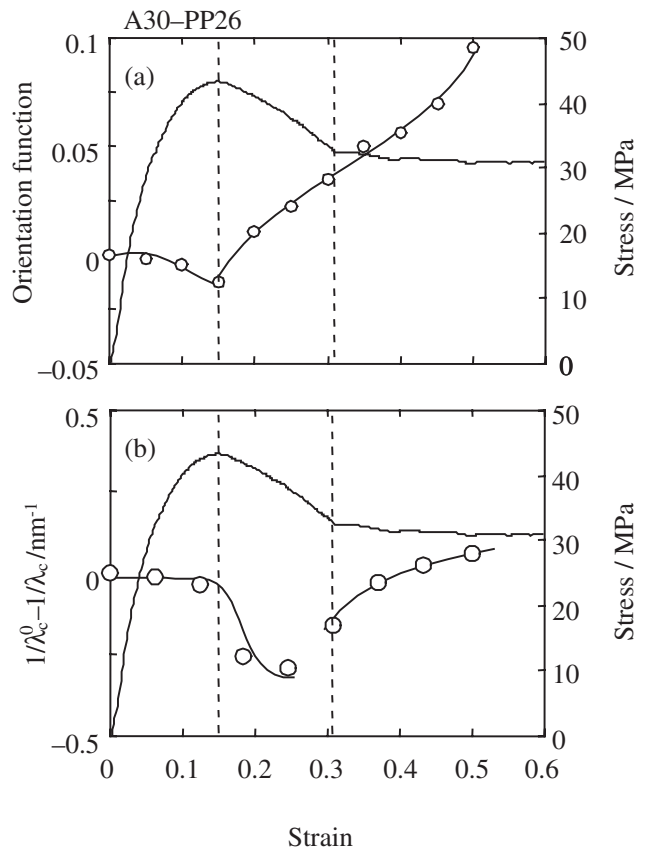
tiated, suggesting a stress- or strain-induced crystallization process of amorphous chains. The important conclusion that is drawn from the major difference between Figures 10b and 14 is that the yield process is associated with the fragmentation process of crystalline lamellae. The present data seems to be analyzed based on the lamellar cluster theory presented by Nitta–Takayanagi.[23,24] Details of the yield process of PP samples will appear in near future.

CONCLUSIONS

In this work we have presented the features of the tensile properties of isotactic polypropylenes at room temperature in the range from glass transition and melting temperatures and have shown how they depend on the independent structural factors such as the lamellar thickness, the amorphous layer thickness, and the spherulite radius. The stress–strain curves for a set of polypropylene solids are typical and display a stress maximum corresponding to a yield point. However the values of yield stress and initial modulus decrease and the yield peak becomes more diffuse as the crystallinity decreases. Spherulites are deformed in the pre-yield region, and the lamellae are destroyed
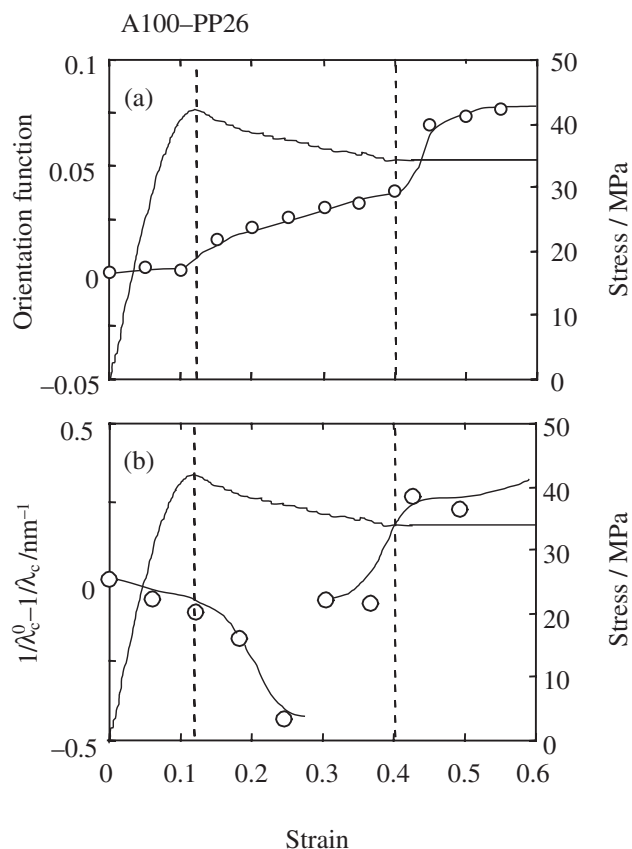
A100–PP26

Figure 12. (a) Orientation function of *c*-axis and (b) changes in lateral lamellar size plotted against strain for A100-PP26. The solid curves denote the stress–strain curves.

at yield point and spherulitic structure are transformed into a highly oriented fibrillar morphology. After the yield drop, a neck was initiated, after which there is a region where the stress remains constant. In the plateau region, the deformation is inhomogeneous and the neck propagates along the specimen.

An important conclusion that can be made from the present study is that the stress–strain curves in the pre-yield region is independent of the size of spherulite when the comparison is made at similar crystalline and amorphous layer thicknesses. In addition, we found the relatively weak dependence of crystallite thickness on the initial modulus and stress, and the strong influence on interlamellar spacing. Therefore the increase in the Young's modulus and stress level with the degree of crystallinity can be attributed to the deformation imposed on the thinner interlamellar region because the modulus of amorphous phase is much lower than that of crystalline phase. Moreover, the tie molecules in the amorphous region where the deformation can be concentrated play important roles in the tensile deformation.
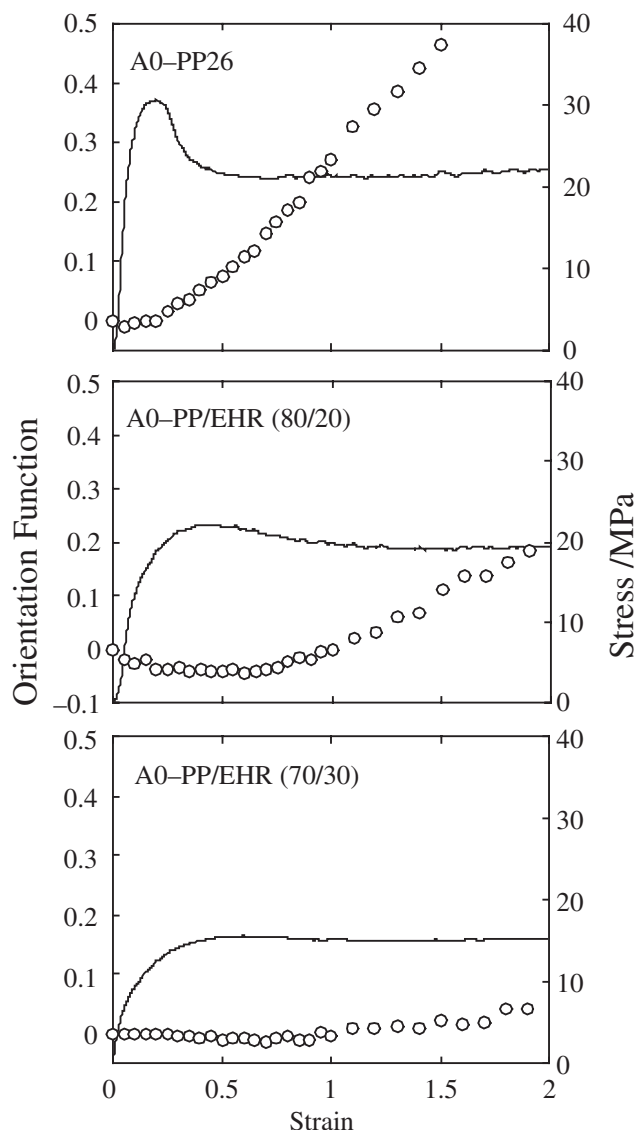
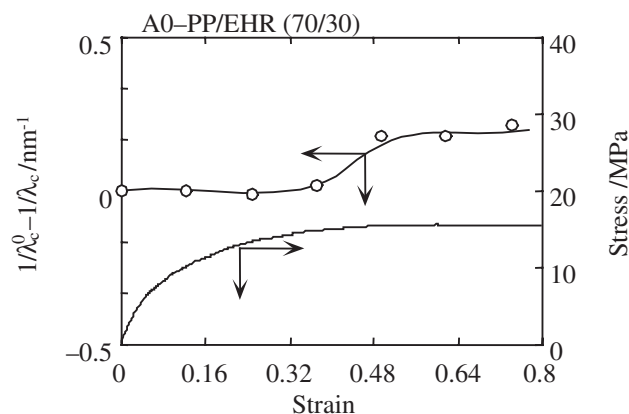**Figure 13.** Comparison of orientation function for PP/EHR samples with different amorphous layer thicknesses.

Figure 14. Change in lateral lamellar size plotted against strain for A-PP/EHR (70/30). The solids curve denotes the stress–strain curve.

REFERENCES

1. R. Popli and L. Mandelkern, *J. Polym. Sci., Polym. Phys. Ed.*, **25**, 441 (1987).
2. L. Mandelkern, *Polym. J.*, **17**, 337 (1985).
3. M. A. Kennedy, A. J. Peacock, and L. Mandelkern, *Macromolecules*, **17**, 5297 (1994).
4. M. A. Kennedy, A. J. Peacock, M. D. Failla, J. C. Lucas, and L. Mandelkern, *Macromolecules*, **28**, 1407 (1995).
5. J. Karger-Kocsis, "Polypropylene: Structure, Blends and Composites," London, Chapman & Hall, 1995.
6. M. Yamaguchi, H. Miyata, and K. Nitta, *J. Appl. Polym. Sci.*, **62**, 87 (1996).
7. M. Yamaguchi, K. Nitta, H. Miyata, and T. Masuda, *J. Appl. Polym. Sci.*, **63**, 467 (1996).
8. K. Nitta, K. Okamoto, and M. Yamaguchi, *Polymer*, **39**, 53 (1998).
9. A. T. Jones and J. Cobbold, *J. Polym. Sci.*, **B6**, 539 (1968).
10. R. J. Saqmuels and R. Y. Yee, *J. Polym. Sci.*, A-2, **10**, 385 (1972).
11. R. S. Stein and M. B. Rhodes, *J. Appl. Phys.*, **31**, 1873 (1960).
12. B. Hartmann and R. F. Cole, *Polym. Eng. Sci.*, **23**, 13 (1983).
13. R. S. Stein, in "New Methods of Polymer Characterization," B. Ke, Ed., Wiley, New York, 1968, p 255.
14. G. L. Wilkes, *Adv. Polym. Sci.*, **8**, 91 (1971).
15. H. W. Siesler, *Adv. Polym. Sci.*, **65**, 1 (1984).
16. J. C. Rodriguez-Cabello, M. Alonso, J. C. Merino, and J. M. Pastor, *J. Appl. Polym. Sci.*, **60**, 1709 (1996).
17. B. Monasse and J. M. Haudin, *Colloid Polym. Sci.*, **263**, 822 (1985).
18. E. J. Clark and J. D. Hoffman, *Macromolecules*, **17**, 878 (1984).
19. Y. S. Yadav and P. C. Jain, *Polymer*, **27**, 721 (1986).
20. K. Nitta, *Comput. Theor. Polym. Sci.*, **9**, 19 (1999).
21. K. Nitta and M. Takayanagi, *J. Polym. Sci., Part B: Polym. Phys.*, **37**, 357 (1999).
22. A. Tanaka, M. Fukuda, H. Nagai, and S. Onogi, *J. Polym. Sci., Part B: Polym. Phys.*, **27**, 2283 (1989).
23. K. Nitta and M. Takayanagi, *J. Macromol. Sci. Phys.*, **B42**, 107 (2003).
24. K. Nitta and M. Takayanagi, *J. Polym. Sci., Part B: Polym. Phys.*, **38**, 1037 (2000).